JOURNAL OF SPACECRAFT AND ROCKETS
Vol. 35, No. 1, January–February 1998

Ionization Around a High-Voltage Body in Magnetized Nonflowing Ionospheric Plasma

Mengu Cho*
Kyushu Institute of Technology, Tobata-ku, Kitakyushu 804, Japan

The electron sheath structure around a cylindrical body with a finite length that is biased to a high positive potential in a magnetized nonflowing ionospheric plasma with enhanced neutral density is studied. The results of Monte-Carlo particle-in-cell simulations show that the sheath boundary increases as the neutral density increases and ionization occurs inside the sheath. There is a critical neutral density above which the sheath expands infinitely, i.e., sheath explosion. A formula of the critical neutral density is derived through theoretical formulation. The theoretical results are compared with the results of the simulation, which serves as a numerical experiment, to check the validity of various assumptions made to derive a simple formula for the critical neutral density. The theoretical formula predicts that the critical neutral density lies in a narrow range of $6 \times 10^{16} \sim 6 \times 10^{17}$ m^{-3}, leaving little dependence on the spacecraft surface potential at typical ionospheric conditions.

Nomenclature

a = nondimensional parameter, $\sqrt{[e\phi_p/(m_e\omega_{ce}^2)]}/r_p$

B = magnetic field strength, G

b = nondimensional parameter, ω_{ce}/ω_{pe}

c = nondimensional parameter, $E_I/e\phi_p$

E_I = threshold value of impact energy for ionization collision rate to be nonzero, eV

I_{eo} = total electron current to upper half body of spacecraft, A

L = axial half length of trapped zone, m

L_c = axial half length of spacecraft, m

m = particle mass, kg

n = particle number density, m^{-3}

n_{nc} = critical neutral density, m^{-3}

q = charge of one superparticle

r_c = electron collection radius, m

r_I = ionization radius, m

r_L = radial boundary position, m

r_{PM} = Parker–Murphy radius, m

r_p = spacecraft body radius, m

r_s = sheath boundary radius, m

T_{eo} = ambient electron temperature, K

v_o = electron thermal flux velocity, m/s

v_{rsi} = secondary ion radial velocity, m/s

w = nondimensional ionization radius, r_I/r_p

x = nondimensional sheath radius, r_s/r_p

y = nondimensional collection radius, r_c/r_p

z_L = axial boundary position, m

Γ_{er} = electron radial flux, 1/m^2/s

Γ_{ez} = electron axial flux, 1/m^2/s

λ_d = debye length, m

ν_{es} = effective scattering frequency, s^{-1}

σ_i = ionization collision cross section, m^2

$\langle\sigma_i v_e\rangle$ = ionization collision rate averaged over electron velocity distribution function, m^3 s^{-1}

ϕ = electric potential, V

ϕ_p = spacecraft body surface potential, V

ω_{ce} = electron gyrofrequency, rad/s

ω_{pe} = electron plasma frequency, rad/s

Subscripts

ai = ambient ion

e = electron

n = neutral

si = secondary ion

Introduction

THIS paper is the second half of a report that presents the results of theoretical and computational works on the sheath structure around a cylindrical body with a finite length that has a high positive potential of the order of 100 V in ionospheric nonflowing magnetoplasma conditions. The cylindrical body simulates a spacecraft in low Earth orbit, although I neglect its orbital motion. The first half of the report is presented in Ref. 1, where I conducted a theoretical formulation on the electron density and the potential structure inside the sheath at the limit of low neutral density and where the neutral density around the object is equal to the ambient undisturbed values. The purpose of this paper is to study the effects of enhanced neutral density on the sheath structure around a cylindrical body with a high positive potential.

In Ref. 1, I studied the electric sheath structure around a cylindrical body with a high positive potential on the order of 100 V. The cylindrical body had its axis parallel to the magnetic field. It was found that the electron density near the surface parallel to the magnetic field, called side surface, can be approximated by a uniform density. Near the side surface, the electrons are trapped by the potential well when they lose their energy by scattering due to collective action of the plasma. The formulas for the uniform electron density and the radius of sheath boundary at the center of cylinder length were derived and checked against computer simulation results. Those formulas form the basis of this paper.

The neutral density around a spacecraft is significantly enhanced when it is emitting various neutral gases into space by thruster firing or outgassing. One report shows the neutral density around the spacecraft can increase as high as 10^{18} m^{-3} when the thruster is fired for attitude control.[2] This number becomes higher as we look at a point closer to the neutral contamination source. In such a situation, if there is a mechanism that destabilizes the sheath structure, such as ionization, a large transient current can flow into the spacecraft, having various undesired side effects on spacecraft operation, such as electromagnetic interference or surface deterioration.

Cho[3] studied the electric sheath structure around a cylinder with an infinite length whose surface was biased to a high positive potential and surrounded by a water vapor cloud in an ionospheric plasma, although the magnetic field and the orbital motion were neglected. The sheath boundary in the radial direction was determined so the negative charge inside the sheath canceled the positive potential of the cylinder. When the cylinder was surrounded by a neutral cloud and ionization occurred inside the sheath, secondary ions accumulated inside the sheath because they move slower than secondary electrons. The sheath boundary expanded outward to balance the

---

Received March 13, 1997; revision received Sept. 26, 1997; accepted for publication Oct. 14, 1997. Copyright © 1997 by the American Institute of Aeronautics and Astronautics, Inc. All rights reserved.

*Associate Professor, Department of Electrical Engineering. E-mail: cho@ele.kyutech.ac.jp. Member AIAA.

increase of the positive charge. As the neutral density increased, there were more secondary ions and the sheath had to collect more electrons from the ambient plasma by extending the boundary further. But this further increased the probability of ionization inside the sheath by increasing the path length for the electrons to travel from the sheath edge to the cylindrical body. Above a certain neutral density, the degree of ionization reached a value so large that the increase of positive charge could not be balanced no matter how far the sheath boundary expanded to collect more electrons. This neutral density is defined as the critical neutral density for sheath explosion.

In Ref. 3, an expression for the critical neutral density for the sheath explosion was derived by solving a set of cold fluid equations. Cho[3] showed that, for typical ionospheric plasma conditions, the critical neutral density was between 10^{16} and 10^{18} m^{-3} for surface potential below 10,000 V. One-dimensional Monte Carlo particle-in-cell (MC-PIC) simulation was done to check the validity of the expression, and simulation results showed that the expression gave a reasonable prediction of the critical neutral density.

Cooke and Katz[4] studied the case of spherical and planar geometries without magnetic field. From the one-dimensional fluid simulation, Cooke and Katz[4] showed that the critical neutral density was in the range $10^{16} \sim 10^{17}$ m^{-3} near 1000 V. Singh and Jaggernauth[5] studied one-dimensional spherical geometry with a one-dimensional fluid simulation code. They studied the unsteady time development of the current collection by a conducting spherical body biased to 140 V in the enhanced neutral gas environment of $\sim 2.4 \times 10^{17}$ m^{-3}.

In this paper, I study the two-dimensional sheath structure around a cylindrical body with a finite length in nonflowing ionospheric plasma with geomagnetic field. I examine whether the conclusions of Refs. 3–5 are still valid when I include the magnetic field.

This paper is divided into two parts. The first part describes the result of particle simulation to study the effect of ionization on the sheath structure. I use an MC-PIC code to show that the electric sheath expands outward because of ionization. In the second part, I derive a formula for the critical neutral density for the sheath explosion. It is possible to calculate the critical neutral density for a given set of parameters, $\phi_p, n_o, \kappa T_{eo}, r_p$, and B, by running many cases of particle simulations. Unfortunately, such a practice is still too expensive even with today's computer technology. In the second part of this paper, therefore, I make many assumptions and approximations to derive a simple formula that can calculate n_{nc} within seconds by a desktop personal computer and can allow study of a wide range of combinations of the parameters. To evaluate the accuracy of the assumptions and approximations, the MC-PIC simulations are used as numerical experiments. The final results of the critical neutral densities calculated by the analytical formula are compared with the results of MC-PIC simulations.

MC-PIC Simulation

Simulation Code

The MC-PIC code used in this paper is the same as the one used in Ref. 1. The computational domain is filled with water vapor of uniform density n_n. I consider a case where the neutral density around spacecraft is enhanced due to various causes, such as thruster firing and surface outgassing. Water is chosen as the neutral species because it is well known to be one of the largest contributors to outgassing on spacecraft.[6] Although the MC-PIC simulation is conducted with the cross-section data of water vapor, the theoretical formulation derived here is applicable to any neutral species as long as it has an ionization rate similar to that of water shown in Fig. 1. Also, the simulation with the cross-section data of other species should give rise to results qualitatively similar to results with water.

I consider collision cross sections of electron-neutral and ion-neutral collision as realistic as possible and include elastic, excitation, attachment, ionization, and charge exchange effects. With more realistic collision cross-section data, better quantitative agreement between the experiment and simulations is possible. In Fig. 1, I show the ionization collision rate, which is the product of the collision cross section and the electron speed, against the electron impact energy. The data are taken from a recommended data set for electron and H_2O collision by Hayashi.[7] Note that $\sigma_i v_e$ is almost constant at impact energies larger than 50 eV. The details of the other collision cross-section data and their test against available swarm experiment data are discussed.[8] The MC-PIC code can reproduce the swarm experiment data for ionization coefficient and electron and ion drift velocities within the maximum error of 10% (Ref. 8).

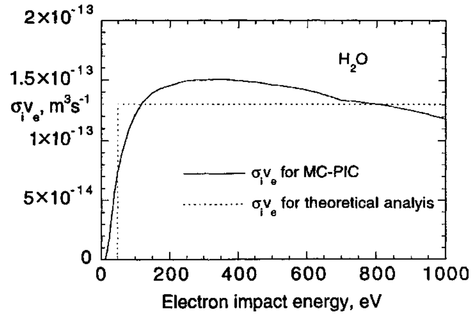

Fig. 1 Ionization collision rate of water vapor.

In the MC-PIC simulation, I follow the motion of many superparticles, which represent groups of real particles. For the ion-to-electron mass ratio, I use $m_{ai}/m_e = 10$ for the ambient ions that fill the computational domain initially and are injected from the top and side boundaries. I use $m_{si}/m_e = 100$ for the secondary ions that are produced by ionization. The real mass ratio of secondary ion to electron is 33,033 for water vapor. To simulate the space charge effects of the secondary ions correctly, the charge-to-mass ratio of the superparticles simulating the secondary ions is set to $q_{si} = \sqrt{(33033/100)}|q_e|$. The detail of this assumption is documented.[8] This treatment of q_{si} is correct to simulate the steady state but incorrect to follow the unsteady development of ionization-driven sheath expansion as studied in Refs. 4 and 5. The low mass ratio of m_{si} still gives the same space charge effect as the real mass ratio as long as the correction on q_{si} is made. In Ref. 9, the one-dimensional simulations with the real mass ratio of m_{si} were compared with the one-dimensional simulations with various m_{si} values, and they gave the same space charge effect, although their timescale varied according to the square root of m_{si}. For the ambient ion, the charge of each superparticle is equal to the absolute value of the electron charge, i.e., $q_{ai} = |q_e|$.

Initially the simulation space is filled with electrons and ions of Maxwellian distribution of $\kappa T_{eo}(=0.2$ or 0.1 eV) and $\kappa T_i(=0.1$ eV) and density n_o. The grid sizes are $\Delta z = \Delta r = 0.02$ m for $n_o = 10^{11}$ m^{-3} and $\Delta z = \Delta r = 0.04$ m for $n_o = 10^{10}$ m^{-3}, which correspond to $\Delta z/\lambda_{de} \leq 2$. The total number of superparticles that initially fill the simulation space is from 10^5 to 10^6 for each species, which depends on the size of simulation space but is set so that at least 10 particles are placed in one grid cell.

The body potential is suddenly raised to a nonzero value ϕ_p at time $t = 0$ and fixed to this value after $t = 0$. If the sheath explosion does not occur, the sheath structure reaches a steady state after initial disturbance. Typically the MC-PIC code is run up to $t = 300\pi/\omega_{pe}$ with the time step of $\Delta t = 0.02/\omega_{pe}$. For all of the cases simulated in this paper, if the steady state is reached, the parameters reach the steady values by this time. If the steady state is not reached and the sheath explosion occurs, the sheath explosion occurs earlier than this time.

MC-PIC Simulation Results

In Fig. 2, I show the potential contours around a cylinder for case (1) with different n_n while keeping the other parameters the same. In Table 1 I list the parameters used for the MC-PIC simulations. The cases shown in Figs. 2a–2g use the same parameters listed for case (1) in Table 1 except the neutral density. In Fig. 2, the shaded area denotes the cylinder body. I show the contours of $\phi = 0.2$, 1, and 10 V. The contour of $\phi = 0.2$ V cannot be well-defined because the plasma oscillation causes fluctuations in the potential structure near $e\phi = \kappa T_{eo}$. As the neutral density around the cylindrical body is increased, charged particle and neutral collision effects become evident. At $n_n = 1 \times 10^{17}$ m^{-3}, the effect of collisions on the sheath structure is still small and the degree of ionization inside the sheath is low. The sheath structure is more or less the same as for $n_n = 1.0 \times 10^{15}$ m^{-3}. The sheath expands slightly at $n_n = 2.0 \times 10^{17}$ m^{-3} if we look at the crossing point of $\phi = 1$ V contour on the r axis. Until $n_n = 9.0 \times 10^{17}$ m^{-3}, the sheath keeps increasing. The expansion occurs in the axial direction as well as in the radial direction.

The sheath expansion in Fig. 2 is due mainly to ionization inside the sheath. I ran the MC-PIC simulation again with $n_n = 9.0 \times 10^{17}$ m^{-3} shown in Fig. 2f but artificially set the ionization collision cross section to zero and kept all of the other collision data the same. The result is shown in Fig. 2h. Because all of the other collision data were the same as in Fig. 2f, electron transport across the magnetic field due to collisional scattering still occurred for this case and electrons were trapped by losing their energy by collision as well as by collective action of the plasma. The potential contours are similar to the lower neutral density case. Therefore, the main cause of the sheath boundary being pushed outward for Fig. 2f is the positive charge of secondary ions produced by ionization.

Up to $n_n = 9.0 \times 10^{17}$ m^{-3}, the sheath structures shown in Fig. 2 are at steady state. At $n_n = 1.0 \times 10^{18}$ m^{-3}, however, the steady state cannot be obtained. The potential contours shown in Fig. 2g are a snapshot of the electric potential distribution at $\omega_{pe}t = 531$ before the simulation is terminated. At $n_n = 1.0 \times 10^{18}$ m^{-3}, there is a region next to the side surface where the potential is higher than the body potential $\phi_p = 100$ V. This region results from secondary ions produced by ionization. The secondary ions move slower than the secondary electrons, giving additional positive charge, and the sheath explosion has been observed for all of the cases listed in Table 1.

In column 2 of Table 2, I list the critical neutral density calculated by the MC-PIC simulations for each case listed in Table. 1. The value listed is the mean value between the highest neutral density where there is a steady sheath without sheath explosion and the lowest neutral density where there is a sheath explosion. In column 2 of Table 2, the ± value indicates the upper and the lower limit on n_{nc}.

Table 1 Parameters of MC-PIC simulation

Case	n_o, m^{-3}	B, G	r_p, m	L_c, m	ϕ, V	κT_{eo}, eV
1	10^{11}	0.35	0.48	0.48	100	0.2
3	10^{11}	0.35	0.48	0.48	200	0.2
4	10^{11}	0.35	0.48	0.96	100	0.2
5	10^{11}	0.35	0.48	0.96	200	0.2
6	10^{11}	0.35	0.96	0.48	100	0.2
7	10^{10}	0.35	0.48	0.96	100	0.1
8	10^{10}	0.35	0.48	0.96	200	0.1
9	10^{10}	0.35	0.48	0.96	300	0.1
10	10^{10}	0.35	0.48	0.96	400	0.1
11	10^{10}	0.35	0.48	1.92	100	0.1
12	10^{11}	0.35	0.24	0.48	100	0.2
13	10^{11}	0.35	0.48	0.48	300	0.2

Theoretical Formulation

I now derive a formula for the critical neutral density for the case of a cylindrical body with a finite length in nonflowing magnetized plasma. I consider the critical neutral density for the direction perpendicular to the magnetic field. The presence of the magnetic field affects the sheath expansion in two opposite ways. On the one hand, it increases the probability of ionization for a given radial distance because electrons rotate in the azimuthal direction by $E \times B$ drift, and the electron path length is longer than in cases when no magnetic field is present and electrons move toward the body surface. Therefore, this effect works to expand the sheath by increasing the positive charge inside the sheath. On the other hand, the magnetic field restricts the radial motion of electrons, and electrons move more slowly in the radial direction than when there is no magnetic field. This effect works to prevent the sheath from expanding by increasing the amount of negative charge inside the sheath. One purpose of this paper is to study whether the overall effect of the magnetic field works to help sheath expansion and lower the critical neutral density or prevents sheath expansion and raises the critical neutral density.

Basic Equations

The sheath boundary is determined by the balance between the positive and negative charges. I consider the volume of trapped zone near $z = 0$, which is defined in Fig. 7 of Ref. 1. Because it is referred to many times in the following discussion, I reproduce it here as Fig. 3. In Fig. 3, an electron whose radial position at $z = z_s$ within the radius r_c is collected directly by the body before it reaches $z = L$. As the positive charge, I consider ambient ions that originate outside the sheath boundary and the secondary ions produced by ionization collision between electrons and neutrals inside the sheath. As the negative charge, I consider electrons that are trapped by the

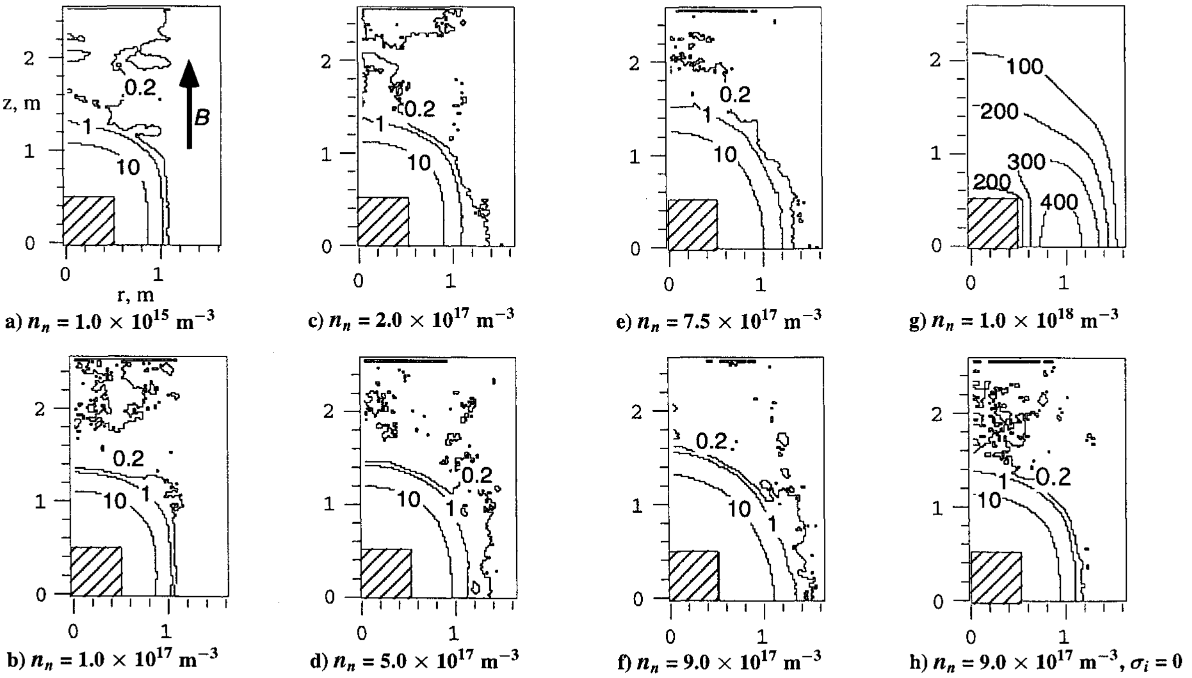

a) $n_n = 1.0 \times 10^{15}$ m^{-3}
c) $n_n = 2.0 \times 10^{17}$ m^{-3}
e) $n_n = 7.5 \times 10^{17}$ m^{-3}
g) $n_n = 1.0 \times 10^{18}$ m^{-3}
b) $n_n = 1.0 \times 10^{17}$ m^{-3}
d) $n_n = 5.0 \times 10^{17}$ m^{-3}
f) $n_n = 9.0 \times 10^{17}$ m^{-3}
h) $n_n = 9.0 \times 10^{17}$ m^{-3}, $\sigma_i = 0$

Fig. 2 Potential structure for different values of n_n of case (1).

Table 2 Results of MC-PIC simulation and theory

	MC-PIC simulation results				Theoretical results				
Case	n_{nc}, 10^{17} m^{-3}	r_s, m	r_c, m	r_I, m	n_{nc}, 10^{17} m^{-3} [Eq. (40)]	r_s, m [Eq. (46)]	r_c, m [Eq. (44)]	r_I, m [Eq. (35)]	n_{nc}, 10^{17} m^{-3} [Eq. (40)]
1	9.5 ± 0.5	1.10	1.06	0.62	4.2	1.14	1.07	0.65	3.2
3	5.5 ± 0.5	1.27	1.13	0.78	2.9	1.35	1.24	0.87	2.8
4	8.3 ± 0.7	1.09	0.93	0.63	2.2	1.14	1.07	0.65	3.2
5	5.5 ± 0.5	1.29	1.24	0.80	4.1	1.34	1.24	0.87	2.8
6	6.3 ± 1.2	1.66	1.41	1.08	1.3	1.73	1.66	1.16	2.4
7	8.3 ± 0.7	1.32	0.98	0.68	1.5	1.35	1.07	0.69	1.7
8	4.5 ± 0.5	1.64	1.19	0.90	1.4	1.64	1.24	0.98	1.4
9	3.5 ± 0.5	1.84	1.29	1.10	1.2	1.85	1.35	1.19	1.2
10	3.5 ± 0.5	2.08	1.40	1.26	1.1	2.03	1.44	1.37	1.1
11	8.8 ± 1.2	1.44	0.97	0.69	1.0	1.35	1.07	0.69	1.7
12	13 ± 1.0	0.77	0.72	0.34	5.5	0.8	0.72	0.37	3.9
13	4.5 ± 0.5	1.39	1.27	0.90	3.4	1.49	1.35	1.02	2.6

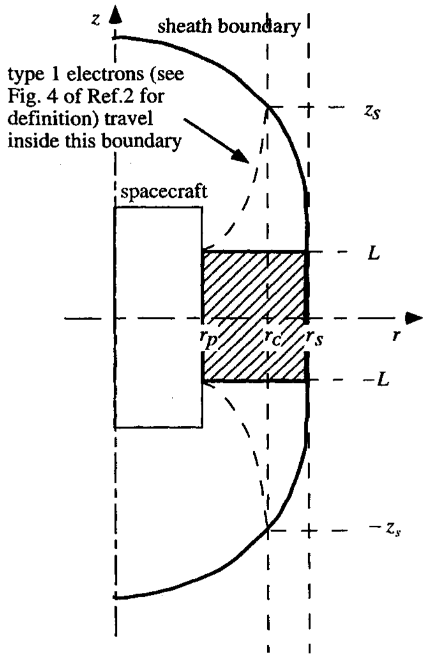

Fig. 3 Volume of trapped zone.

potential well by losing their energy by collision or by collective action of the plasma (type 4 electrons in Ref. 1) and secondary electrons produced by ionization. Integrating the Poisson equation in cylindrical coordinates with azimuthal symmetry,

$$\int_{-L}^{+L}\left(r_s\frac{\partial\phi}{\partial r}\bigg|_{r=r_s}-r_p\frac{\partial\phi}{\partial r}\bigg|_{r=r_p}\right)\mathrm{d}z + \int_{r_p}^{r_s}\left(\frac{\partial\phi}{\partial z}\bigg|_{z=-L}-\frac{\partial\phi}{\partial z}\bigg|_{z=+L}\right)r\,\mathrm{d}r = \int_{-L}^{+L}\int_{r_p}^{r_s}\frac{-e}{\epsilon_o}(n_{si}+n_{ai}-n_e)r\,\mathrm{d}r\,\mathrm{d}z \tag{1}$$

At the sheath boundary I impose the following boundary conditions:

$$\phi|_{r=r_s}=0 \tag{2}$$

$$\frac{\partial\phi}{\partial r}\bigg|_{r=r_s}=0 \tag{3}$$

$$n_{ai}|_{r=r_s}=n_e|_{r=r_s} \tag{4}$$

Justification of Eqs. (2) and (3) is given in Ref. 1.

At the sheath boundary, the radial electric field is zero. Therefore, the first term in the first integral of the left-hand side of Eq. (1) is 0. As shown in the potential contour plot in Fig. 2a, the potential contour is almost parallel to the z direction near the side surface. Therefore, the tangential electric field is much smaller than the radial electric field at the surface $r=r_p$ and I neglect the second integral compared with the first integral in the left-hand side of Eq. (1). Therefore, only the second term in the first integral in the left-hand side and the right-hand side of Eq. (1) remains, and they are rewritten as

$$\int_{-L}^{+L}-r_p\frac{\partial\phi}{\partial r}\bigg|_{r=r_p}\mathrm{d}z=\int_{-L}^{+L}\int_{r_p}^{r_s}\frac{-e}{\epsilon_o}(n_{si}+n_{ai}-n_e)r\,\mathrm{d}r\,\mathrm{d}z \tag{5}$$

For a given set of ϕ_p and r_p, both sides of Eq. (5) are functions of n_n and r_s. The total differential of Eq. (5) can be written as

$$\begin{aligned}&\frac{\partial}{\partial r_s}\left(\int_{-L}^{+L}-r_p\frac{\partial\phi}{\partial r}\bigg|_{r=r_p}\mathrm{d}z\right)\mathrm{d}r_s\\&+\frac{\partial}{\partial n_n}\left(\int_{-L}^{+L}-r_p\frac{\partial\phi}{\partial r}\bigg|_{r=r_p}\mathrm{d}z\right)\mathrm{d}n_n\\&=\frac{\partial}{\partial r_s}\left[\int_{-L}^{+L}\int_{r_p}^{r_s}\frac{-e}{\epsilon_o}(n_{si}+n_{ai}-n_e)r\,\mathrm{d}r\,\mathrm{d}z\right]\mathrm{d}r_s\\&+\frac{\partial}{\partial n_n}\left[\int_{-L}^{+L}\int_{r_p}^{r_s}\frac{-e}{\epsilon_o}(n_{si}+n_{ai}-n_e)r\,\mathrm{d}r\,\mathrm{d}z\right]\mathrm{d}n_n\end{aligned} \tag{6}$$

Rewriting this equation, I obtain

$$\frac{\mathrm{d}r_s}{\mathrm{d}n_n}=\frac{-\dfrac{\partial}{\partial n_n}\left(\displaystyle\int_{-L}^{+L}-r_p\frac{\partial\phi}{\partial r}\bigg|_{r_p}\mathrm{d}z\right)+\dfrac{\partial}{\partial n_n}\left[\displaystyle\int_{-L}^{+L}\int_{r_p}^{r_s}\frac{-e}{\epsilon_o}(n_{si}+n_{ai}-n_e)r\,\mathrm{d}r\,\mathrm{d}z\right]}{\dfrac{\partial}{\partial r_s}\left(\displaystyle\int_{-L}^{+L}-r_p\frac{\partial\phi}{\partial r}\bigg|_{r_p}\mathrm{d}z\right)-\dfrac{\partial}{\partial r_s}\left[\displaystyle\int_{-L}^{+L}\int_{r_p}^{r_s}\frac{-e}{\epsilon_o}(n_{si}+n_{ai}-n_e)r\,\mathrm{d}r\,\mathrm{d}z\right]} \tag{7}$$

This gives the degree of sheath expansion for a unit increase of the neutral density.

The sheath explosion occurs when the denominator of the above equation is zero and $\mathrm{d}r_s/\mathrm{d}n_n$ approaches infinity. Therefore, the condition for the sheath explosion is written as

$$\frac{\partial}{\partial r_s}\left(\int_{-L}^{+L} -r_p \left.\frac{\partial\phi}{\partial r}\right|_{r_p} \mathrm{d}z\right)$$

$$-\frac{\partial}{\partial r_s}\left[\int_{-L}^{+L}\int_{r_p}^{r_s}\frac{-e}{\epsilon_o}(n_{si}+n_{ai}-n_e)r\,\mathrm{d}r\,\mathrm{d}z\right]=0 \tag{8}$$

I assume that all of the parameters included in Eq. (8) are uniform in the z direction in the volume defined in Fig. 3. Then, the integral with respect to z can be removed from Eq. (8) and the condition for the sheath explosion can be obtained as

$$\frac{\partial}{\partial r_s}\left(r_p\left.\frac{\partial\phi}{\partial r}\right|_{r_p}\right)+\frac{-e}{\epsilon_o}\left(\frac{\partial}{\partial r_s}\int_{r_p}^{r_s} n_{si}r\,\mathrm{d}r\right.$$

$$\left.+\frac{\partial}{\partial r_s}\int_{r_p}^{r_s} n_{ai}r\,\mathrm{d}r-\frac{\partial}{\partial r_s}\int_{r_p}^{r_s} n_e r\,\mathrm{d}r\right)=0 \tag{9}$$

Now the problem has been reduced to a one-dimensional problem in the r direction. Basically this condition is the same for the sheath explosion discussed in Ref. 3 for the one-dimensional unmagnetized cylindrical case. An equation similar to Eq. (9) can be obtained by setting the denominator to 0 in Eq. (15) of Ref. 3. The difference from Ref. 3 is that the particle densities n_{ai}, n_{si}, and n_e now depend on the magnetic field strength.

Particle Density Inside the Sheath

I now consider a way to evaluate the integrals of $n_{si}r$, $n_{ai}r$, and $n_e r$ in Eq. (9). For the integrals of the ambient ion density and the electron density, I can write

$$\frac{\partial}{\partial r_s}\int_{r_p}^{r_s} n_{ai}r\,\mathrm{d}r = n_{ai}|_{r=r_s}r_s+\int_{r_p}^{r_s}\frac{\partial n_{ai}}{\partial r_s}r\,\mathrm{d}r \tag{10}$$

$$\frac{\partial}{\partial r_s}\int_{r_p}^{r_s} n_e r\,\mathrm{d}r = n_e|_{r=r_s}r_s+\int_{r_p}^{r_s}\frac{\partial n_e}{\partial r_s}r\,\mathrm{d}r \tag{11}$$

Regarding the secondary ion density at a radius r, I divide the ions into multiple groups depending on their points of production. A group of secondary ions is produced at the rate of $n_e n_n\langle\sigma_i v_e\rangle 2\pi r'\,\mathrm{d}r'\,\mathrm{d}z$ per unit time between $r'-\mathrm{d}r'$ and r', where $\langle\sigma_i v_e\rangle$ is the ionization collision rate at point r', which is given by taking the average of the product of the ionization collision cross section σ_i and the electron velocity v_e over the electron velocity distribution function. I denote the number density of those secondary ions at point r by $\delta n_{si}(r', r)$. I assume that this group of ions is produced only between $r'-\mathrm{d}r'$ and r'. I neglect the axial velocity of secondary ions compared with their radial velocity. Then its flow rate $\delta n_{si}v_{rsi}2\pi r\,\mathrm{d}z$ is constant at $n_e n_n\langle\sigma_i v_e\rangle 2\pi r'\,\mathrm{d}r'\,\mathrm{d}z$ for $r > r'$. The secondary ions are accelerated to $v_{rsi}(r', r)$ while they move from r' to r. Then the following continuity and momentum equations can be written as

$$\delta n_{si}(r', r)v_{rsi}(r', r)2\pi r = n_e n_n\langle\sigma_i v_e\rangle 2\pi r'\,\mathrm{d}r' \qquad (r > r') \tag{12}$$

$$\frac{1}{r}\frac{\partial}{\partial r}\left[\delta n_{si}(r', r)v_{rsi}(r', r)^2 r\right]=\delta n_{si}(r', r)\frac{e}{m_{si}}\left(-\frac{\partial\phi}{\partial r}\right) \tag{13}$$

where I neglect the pressure term of the secondary ions compared with the electrostatic acceleration. I also neglect the effect of collision on the secondary ion motion because the collision probability is very small for this case. Substituting the continuity equation into the momentum equation [Eq. (13)], and integrating it from r' to r, I obtain

$$v_{rsi}(r', r)=\sqrt{(2e/m_{si})}\sqrt{\phi(r')-\phi(r)} \tag{14}$$

The total secondary ion density at a point r is given as the sum of all the groups produced between r_p and r. I substitute Eq. (14) into Eq. (12) and obtain the total secondary ion density at point r as

$$n_{si}(r)=\int\delta n_{si}(r', r)=\int_{r_p}^{r}\frac{n_e n_n\langle\sigma_i v_e\rangle r'\,\mathrm{d}r'}{v_{rsi}(r', r)r}$$

$$=\int_{r_p}^{r}\frac{n_e n_n\langle\sigma_i v_e\rangle r'}{\sqrt{(2e/m_{si})}\sqrt{[\phi(r')-\phi(r)]}r}\,\mathrm{d}r' \tag{15}$$

Therefore, the integral of $n_{si}r$ in Eq. (9) is written as

$$\int_{r_p}^{r_s} n_{si}r\,\mathrm{d}r=\int_{r_p}^{r_s}\int_{r_p}^{r}\frac{n_e n_n\langle\sigma_i v_e\rangle r'}{\sqrt{(2e/m_{si})}\sqrt{\phi(r')-\phi(r)}}\,\mathrm{d}r'\,\mathrm{d}r \tag{16}$$

Critical Neutral Density

I substitute Eqs. (10), (11), and (16) into Eq. (9) and obtain

$$\frac{\partial}{\partial r_s}\left(r_p\left.\frac{\partial\phi}{\partial r}\right|_{r_p}\right)+\frac{-e}{\epsilon_o}\int_{r_p}^{r_s}\left(\frac{\partial n_{ai}}{\partial r_s}-\frac{\partial n_e}{\partial r_s}\right)r\,\mathrm{d}r$$

$$+\frac{-e}{\epsilon_o}\sqrt{\frac{m_{si}}{2e}}\frac{\partial}{\partial r_s}\int_{r_p}^{r_s}\int_{r_p}^{r}\frac{n_e n_n\langle\sigma_i v_e\rangle r'}{\sqrt{\phi(r')-\phi(r)}}\,\mathrm{d}r'\,\mathrm{d}r=0 \tag{17}$$

where the first terms of Eqs. (10) and (11) cancel each other because of charge neutrality at the sheath boundary, i.e., $n_{ai}|_{r=r_s}=n_e|_{r=r_s}$. Because the ambient ion density decreases exponentially inside the sheath, I neglect $(\partial/\partial r_s)n_{ai}$ in the integral of the second term in Eq. (17) compared with $(\partial/\partial r_s)n_e$. I also assume that the neutral density is uniform. Then Eq. (17) can be rewritten in the following form:

$$n_n=\frac{\dfrac{\epsilon_o}{e}\dfrac{\partial}{\partial r_s}\left(r_p\left.\dfrac{\partial\phi}{\partial r}\right|_{r=r_p}\right)+\displaystyle\int_{r_p}^{r_s}\frac{\partial n_e}{\partial r_s}r\,\mathrm{d}r}{\sqrt{\dfrac{m_{si}}{2e}}\dfrac{\partial}{\partial r_s}\displaystyle\int_{r_p}^{r_s}\int_{r_p}^{r}\frac{n_e\langle\sigma_i v_e\rangle r'}{\sqrt{\phi(r')-\phi(r)}}\,\mathrm{d}r'\,\mathrm{d}r} \tag{18}$$

When the neutral density reaches this value, the denominator of Eq. (7) becomes 0 and sheath explosion occurs. Therefore, Eq. (18) is the formula that gives the critical neutral density.

I make various assumptions to simplify Eq. (18) to obtain a formula that can be useful to calculate n_{nc} with the minimum computation time and study its behavior over a wide range of parameters. I first list the five major assumptions used in this section. These assumptions are made only for the parameters inside the volume defined in Fig. 3, i.e., $-L < z < L$ and $r_p < r < r_s$: Assumption (1), all of the parameters are uniform in the z direction inside the volume; Assumption (2), the ionization collision rate $\langle\sigma_i v_e\rangle$ is constant at $\langle\sigma_i v_e\rangle_o$ between r_p and r_I and 0 between r_I and r_s (the radius r_I is the point where $e\phi=E_I$, where E_I is the threshold value for ionization, and I call it the ionization radius in this paper); Assumption (3), the electric potential between r_p and r_s is approximated by

$$\phi(r)=\phi_p\left\{\frac{r_s^2\ln(r_s/r)-\left[\left(r_s^2-r^2\right)/2\right]}{r_s^2\ln(r_s/r_p)-\left[\left(r_s^2-r_p^2\right)/2\right]}\right\} \tag{19}$$

Assumption (4), the electron density between r_p and r_s is uniform.

Assumptions (1) and (4) are justified by looking at the potential and electron density near the body surface in the results of MC-PIC simulations. In Fig. 4, I show the distribution of ϕ at $z=0$ line for different values of n_n below the critical neutral density for case (1)

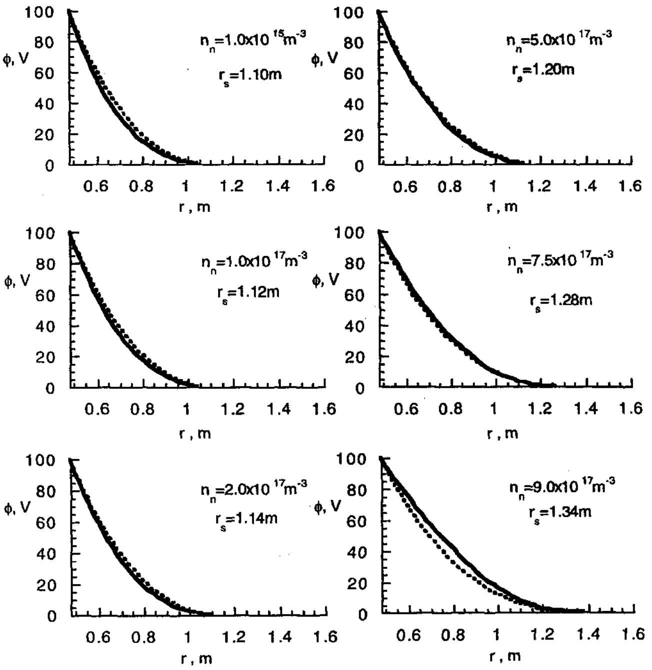

Fig. 4 Electric potential at $z = 0$ for different values of n_n: ——, MC-PIC simulations results and - - - -, Eq. (19).

of MC-PIC simulations by solid lines. I also show the distribution of ϕ calculated from Eq. (19) by dashed lines. Equation (19) assumes that the charge density inside the sheath is uniform between r_p and r_s and the boundary conditions are given by Eqs. (2) and (3) and $\phi = \phi_p$ at $r = r_p$. The same potential distribution was used in Ref. 1 to calculate the electron density inside the sheath. The potential structures shown in Fig. 4 agree very well with Eq. (19), validating Assumption (3).

I use Assumption (3) to approximate the electric field at the cylindrical surface as

$$\left.\frac{\partial\phi}{\partial r}\right|_{r=r_p} = -\frac{\phi_p\left(r_s^2 - r_p^2\right)}{r_p\left\{r_s^2 \ln(r_s/r_p) - \left[\left(r_s^2 - r_p^2\right)/2\right]\right\}} \tag{20}$$

Then the first term in the numerator of Eq. (18) is written as

$$\frac{\epsilon_o}{e}\frac{\partial}{\partial r_s}\left(r_p \left.\frac{\partial\phi}{\partial r}\right|_{r=r_p}\right)$$

$$= \frac{\epsilon_o\phi_p 2r_s\left\{\left[\left(r_s^2 - r_p^2\right)/2\right] - r_p^2 \ln(r_s/r_p)\right\}}{e\left\{r_s^2 \ln(r_s/r_p) - \left[\left(r_s^2 - r_p^2\right)/2\right]\right\}^2} \tag{21}$$

Assumption (2) means that ionization is neglected at the points whose electric potential is low. This is because the ionization collision rate $\langle\sigma_i v_e\rangle$ is very small near the ionization potential. Based on the ionization collision rate shown in Fig. 1, I approximate the ionization rate by 0 for impact energy less than 50 eV and

$$\langle\sigma_i v_e\rangle_o = 1.3 \times 10^{-13}(\mathrm{m}^3\,\mathrm{s}^{-1}) \tag{22}$$

for impact energy larger than 50 eV. Note that E_I is different from the ionization potential, which is 12.7 eV for a water molecule. By using Assumption (3), the radius r_I is given as the solution of the following equation:

$$E_I = e\phi_p\left\{\frac{r_s^2 \ln(r_s/r_I) - \left[\left(r_s^2 - r_I^2\right)/2\right]}{r_s^2 \ln(r_s/r_p) - \left[\left(r_s^2 - r_p^2\right)/2\right]}\right\} \tag{23}$$

Because the ionization collision rate is 0 for $r > r_I$, the integral in the denominator of Eq. (18) is rewritten as

$$\int_{r_p}^{r_s}\int_{r_p}^{r}\frac{n_e\langle\sigma_i v_e\rangle r'}{\sqrt{\phi(r') - \phi(r)}}\,\mathrm{d}r'\,\mathrm{d}r = \int_{r_p}^{r_s}\int_{r_p}^{r}\frac{n_e\langle\sigma_i v_e\rangle_o r'}{\sqrt{\phi(r') - \phi(r)}}\,\mathrm{d}r'\,\mathrm{d}r$$
$$- \int_{r_I}^{r_s}\int_{r_I}^{r}\frac{n_e\langle\sigma_i v_e\rangle_o r'}{\sqrt{\phi(r') - \phi(r)}}\,\mathrm{d}r'\,\mathrm{d}r \tag{24}$$

I give the electron density n_e by

$$n_e = \sqrt{2}n_o\frac{\omega_{ce}}{\omega_{pe}}\sqrt{\frac{r_s^2 - r_c^2}{r_s^2 - r_p^2}} \tag{25}$$

This is Eq. (20) of Ref. 1, where no ionization was taken into account. I still apply this equation even if I now include ionization. Physically, this means that even if ionization inside the sheath increases the electron density in the volume of Fig. 3, its effect is hidden by the effect caused by the increased electron mobility across the magnetic field and the effect caused by the increased trapping probability due to nonionization collision. I take the partial derivative of Eq. (25) with respect to r_s and evaluate the second term in the numerator of Eq. (18). It is written as

$$\int_{r_s}^{r_p}\left(\frac{\partial n_e}{\partial r_s}\right) r\,\mathrm{d}r = \int_{r_s}^{r_p} n_e r_s\left[\frac{1}{\left(r_s^2 - r_c^2\right)} - \frac{1}{\left(r_s^2 - r_p^2\right)}\right] r\,\mathrm{d}r$$
$$= n_e r_s\frac{r_c^2 - r_p^2}{2\left(r_s^2 - r_c^2\right)} \tag{26}$$

Before I proceed further to simplify Eq. (18), I define the following nondimensional parameters:

$$r_s/r_p = x \tag{27}$$

$$r_c/r_p = y \tag{28}$$

$$r_I/r_p = w \tag{29}$$

$$\sqrt{\frac{e\phi_p}{m_e\omega_{ce}^2}}\bigg/ r_p = a \tag{30}$$

$$\omega_{ce}/\omega_{pe} = b \tag{31}$$

$$E_I/e\phi_p = c \tag{32}$$

I substitute Eqs. (21), (24), and (26) into Eq. (18) and rewrite it as

$$n_{nc} = \frac{\dfrac{1}{\langle\sigma_i v_e\rangle_o r_p}\sqrt{\dfrac{2e\phi_p}{m_{si}}}\left(\sqrt{2}a^2 b\dfrac{x\{[(x^2-1)/2] - \ln x\}}{\{x^2 \ln x - [(x^2-1)/2]\}^2} + \dfrac{1}{2}\sqrt{\dfrac{x^2-y^2}{x^2-1}}\dfrac{x(y^2-1)}{(x^2-y^2)}\right)}{\dfrac{\partial}{\partial x}\left\{\sqrt{\dfrac{x^2-y^2}{x^2-1}}\sqrt{x^2 \ln x - \dfrac{x^2-1}{2}}\left[\displaystyle\int_1^x\int_1^\xi \frac{\xi'}{\sqrt{\psi(x,\xi') - \psi(x,\xi)}}\,\mathrm{d}\xi'\,\mathrm{d}\xi - \int_w^x\int_w^\xi \frac{\xi'}{\sqrt{\psi(x,\xi') - \psi(x,\xi)}}\,\mathrm{d}\xi'\,\mathrm{d}\xi\right]\right\}} \tag{33}$$

where $\psi(x, \xi)$ is a nondimensional potential given by

$$\psi(x, \xi) = x^2 \ln\left(\frac{x}{\xi}\right) - \frac{x^2 - \xi^2}{2} \tag{34}$$

and the nondimensional radius w is determined by the following equation [see Eq. 23]:

$$c = \frac{x^2 \ln(x/w) - [(x^2 - w^2)/2]}{x^2 \ln x - [(x^2 - 1)/2]} \tag{35}$$

After some algebra (see Appendix), the integrals in the denominator can be approximated by

$$\int_1^x \int_1^\xi \frac{\xi'}{\sqrt{\psi(x,\xi') - \psi(x,\xi)}}\,\mathrm{d}\xi'\,\mathrm{d}\xi \simeq 0.865\left[\frac{1}{2}\sqrt{x^2-1} + \frac{\pi}{4}x^2 - \frac{x^2}{2}\sin^{-1}\left(\frac{1}{x}\right)\right] \tag{36}$$

$$\int_w^x \int_w^\xi \frac{\xi'}{\sqrt{\psi(x,\xi') - \psi(x,\xi)}}\,\mathrm{d}\xi'\,\mathrm{d}\xi \simeq \frac{\sqrt{2}\pi}{8}(x^2 - w^2) \tag{37}$$

Then I can write

$$\frac{\partial}{\partial x}\left\{\sqrt{\frac{x^2-y^2}{x^2-1}}\sqrt{x^2 \ln x - \frac{x^2-1}{2}} \times\left[\int_1^x \int_1^\xi \frac{\xi'}{\sqrt{\psi(x,\xi') - \psi(x,\xi)}}\,\mathrm{d}\xi'\,\mathrm{d}\xi - \int_w^x \int_w^\xi \frac{\xi'}{\sqrt{\psi(x,\xi') - \psi(x,\xi)}}\,\mathrm{d}\xi'\,\mathrm{d}\xi\right]\right\} = G(x,y,w) \tag{38}$$

where $G(x, y, w)$ is a nondimensional function of x, y, and w given by

$$\begin{aligned} G(x,y,w) = {} & \frac{x(y^2-1)}{(x^2-y^2)^{\frac{1}{2}}(x^2-1)^{\frac{3}{2}}}\sqrt{x^2 \ln x - \frac{x^2-1}{2}} \\ & \times\left\{0.865\left[\frac{1}{2}\sqrt{x^2-1} + \frac{\pi}{4}x^2 - \frac{x^2}{2}\sin^{-1}\left(\frac{1}{x}\right)\right]\right. \\ & \left. - \frac{\sqrt{2}\pi}{8}(x^2-w^2)\right\} + \sqrt{\frac{x^2-y^2}{x^2-1}}\frac{x \ln x}{\sqrt{x^2 \ln x - [(x^2-1)/2]}} \\ & \times\left\{0.865\left[\frac{1}{2}\sqrt{x^2-1} + \frac{\pi}{4}x^2 - \frac{x^2}{2}\sin^{-1}\left(\frac{1}{x}\right)\right]\right. \\ & \left. - \frac{\sqrt{2}\pi}{8}(x^2-w^2)\right\} + \sqrt{\frac{x^2-y^2}{x^2-1}}\sqrt{x^2 \ln x - \frac{x^2-1}{2}} \\ & \times\left\{0.865\left[\frac{x}{\sqrt{x^2-1}} + \frac{\pi}{2}x - x\sin^{-1}\left(\frac{1}{x}\right)\right]\right. \\ & \left. - \frac{\sqrt{2}\pi}{8}\left(2x - 2w\frac{\mathrm{d}w}{\mathrm{d}x}\right)\right\} \end{aligned} \tag{39}$$

I substitute Eq. (39) into Eq. (33) and obtain

$$n_{nc} = \frac{1}{\langle\sigma_i v_e\rangle_o r_p}\sqrt{\frac{2e\phi_p}{m_{si}}}F(x,y,w) \tag{40}$$

where $F(x, y, w)$ is the nondimensional function given by

$$\begin{aligned} & F(x,y,w) \\ & = \left\{\sqrt{2}a^2 b\left[x\left(\frac{x^2-1}{2} - \ln x\right)\Big/\left(x^2 \ln x - \frac{x^2-1}{2}\right)^2\right]\right. \\ & \left. + \frac{1}{2}\sqrt{\frac{x^2-y^2}{x^2-1}}\frac{x(y^2-1)}{(x^2-y^2)}\right\}\Big/ G(x,y,w) \end{aligned} \tag{41}$$

I now have a formula for the critical neutral density, which can be calculated easily once I know the nondimensional sheath radius $x = r_s/r_p$, the nondimensional collection radius $y = r_c/r_p$, and the nondimensional ionization radius $w = r_I/r_p$. These radii should be evaluated at the neutral density just below the critical neutral density. It is very difficult, however, to define r_s and r_c at such a condition even with MC-PIC simulation. As shown in Fig. 4, r_s increases abruptly at the neutral density close to the critical neutral density. Therefore, I approximate r_s and r_c by the values of the cases with a low neutral density where the ionization effect is negligible. I substitute r_s, r_c, and r_I taken from the result of the MC-PIC simulations with $n_n = 10^{15}$ m^{-3} into Eq. (40) and list the result in column 6 of Table 2. In the columns 3–5, I list the values of r_s, r_c, and r_I used to calculate column 6, where I approximate r_c by

$$r_c \simeq \sqrt{\frac{|I_{eo}|}{en_o v_o \pi}} \tag{42}$$

by neglecting the contribution of trapped electrons and heated electrons to the total electron current I_{eo} to the upper half body of the cylinder.

Discussion

The critical neutral densities given by Eq. (40) agree with the actual critical neutral density obtained from the MC-PIC simulation within a factor of 8 for $\phi_p = 100$ V. It agrees better at a high potential of $\phi_p \geq 200$ within a factor of 3. At low potential, Eq. (40) underestimates the critical neutral density. This comes from the use of Assumption (2), which means that ionization takes place everywhere between r_p and r_I at a constant rate of $\langle\sigma_i v_e\rangle_o = 1.3 \times 10^{-13}$ m^3 s^{-1}. For the low potential, $\phi_p \sim 100$ V, this still overestimates the ionization rate, because the ionization collision rate shown in Fig. 1 is less than 1.3×10^{-13} m^3 s^{-1} at an impact energy of less than 120 V. Assumption (2) becomes more realistic at higher ϕ_p where most of the points in $r < r_s$ give a particle energy higher than 120 V. At the lower potential, the degree of overestimation on the ionization rate is severe and leads to underestimation on n_{nc}.

Although I would like to study the dependence of n_{nc} on each parameter of interest, it is very expensive to calculate r_s, r_c, and r_I from the MC-PIC simulations for each case. I therefore consider a way to express n_{nc} without the aid of MC-PIC simulations to define r_s and r_c. First, I approximate the electron collection radius r_c by the so-called Parker–Murphy radius[10]

$$r_{PM} = r_p\left(1 + \sqrt{\frac{8e\phi_p}{m_e\omega_{ce}^2 r_p^2}}\right)^{\frac{1}{2}} \tag{43}$$

When I use r_{PM} as r_c, the nondimensional parameter y is given by

$$y^2 = 1 + 2\sqrt{2}a \tag{44}$$

For the sheath radius r_s, I use the result of Ref. 1, where the sheath radius is given as the solution of the following equation:

$$\phi_p = \frac{e}{\epsilon_o}\frac{n_o}{\sqrt{2}}\frac{\omega_{ce}}{\omega_{pe}}r_p^2\sqrt{\frac{(r_s/r_p)^2 - 1 - \sqrt{\left(8e\phi_p/m_e\omega_{ce}^2 r_p^2\right)}}{(r_s/r_p)^2 - 1}} \times\left[\left(\frac{r_s}{r_p}\right)^2 \ln\left(\frac{r_s}{r_p}\right) - \frac{(r_s/r_p)^2 - 1}{2}\right] \tag{45}$$

This is Eq. (22) of Ref. 1, which neglects the effect of ionization, although the effect of magnetic field is taken into account. Equation (45) is nondimensionalized to yield

$$a^2 b = \frac{1}{\sqrt{2}}\sqrt{\frac{x^2 - 1 - \sqrt{8}a}{x^2-1}}\left(x^2 \ln x - \frac{x^2-1}{2}\right) \tag{46}$$

I calculate x from this equation by an iteration method. The nondimensional ionization radius w is obtained by Eq. (35) with x determined from Eq. (46).

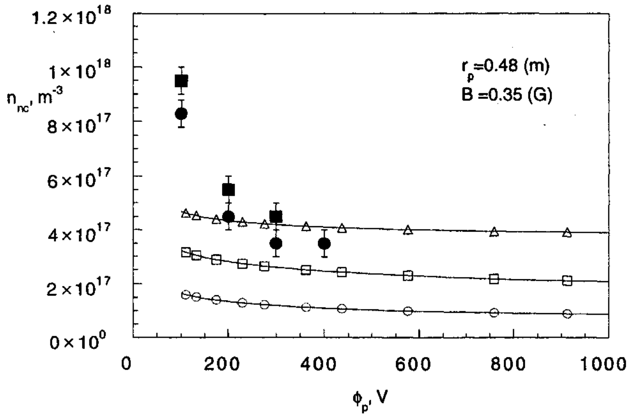

Fig. 5 **Critical neutral density n_{nc} against surface potential ϕ_p for different plasma densities n_o: ○, theory (n_o = 10^{10} m^{-3}); □, theory (n_o = 10^{11} m^{-3}); △, theory (n_o = 10^{12} m^{-3}); ●, simulation (n_o = 10^{10} m^{-3}); and ■, simulation (n_o = 10^{11} m^{-3}).**

I can now calculate the critical neutral density for a given set of m_{si}, $\langle\sigma_i v_e\rangle$, r_p, ϕ_p, and ω_{ce}, which defines a, b, and c and gives x, y, and w from Eqs. (46), (44), and (35). In column 10 of Table 2, I list the critical neutral density calculated this way. I also list r_s, r_c, and r_I in the columns 7–9, which are used to calculate column 10. The critical neutral densities calculated in this way agree with the simulation results within a factor of 6 for low potential $\phi_p = 100$ V and a factor of 3 for higher potential $\phi_p \geq 200$ V. The use of Eq. (44) improves the agreement for low potential $\phi_p = 100$ V compared with column 6 even though I have made more approximations. This is because the use of r_{PM} as r_c, which is the upper limit on r_c, gives an overestimate of r_c and y and leads to an underestimate of the factor $(x^2 - y^2)$, which appears in the denominator of Eq. (33). Therefore, the overestimate caused by the use of Eq. (44) somewhat cancels the underestimate caused by the use of Assumption (2), which is the major reason for the underestimate at the low potential of 100 V.

In Fig. 5, I plot the critical neutral densities against the surface potential ϕ_p for three different plasma densities, which correspond to low, middle, and high density in the ionosphere. I also plot the critical neutral densities obtained from the MC-PIC simulations. At the low potentials, the critical neutral density decreases as the potential increases. This is because, at the low potential, not all of the sheath thickness $r_s - r_p$ is used for ionization. Ionization occurs only at a part of the sheath where $e\phi(r) > E_I$. As the surface potential increases, the nonionization part $r_s > r > r_I$ can be neglected compared with the ionization part $r_I > r > r_p$ and the difference due to this effect diminishes.

At potentials ~1000 V, the critical neutral density stays at a relatively constant value. At high ϕ_p, I can approximate $w \simeq x$ and x^2, $y^2 \gg 1$. Then the dominant term in the numerator of $F(x, y, w)$ in Eq. (41) is the second term, $\frac{1}{2}\surd[(x^2 - y^2)/(x^2 - 1)][x(y^2 - 1)/(x^2 - y^2)]$. At high ϕ_p, this approaches $\frac{1}{2}[y^2/\surd(x^2 - y^2)]$. The dominant term in $G(x, y, w)$ is the first term in Eq. (39). At high ϕ_p, this approaches

$$\frac{x(y^2-1)}{(x^2-y^2)^{\frac{1}{2}}(x^2-1)^{\frac{3}{2}}}\sqrt{x^2\,\ell n x - \frac{x^2-1}{2}}$$

$$\times\left\{0.865\left[\frac{1}{2}\sqrt{x^2-1}+\frac{\pi}{4}x^2-\frac{x^2}{2}\sin^{-1}\left(\frac{1}{x}\right)\right]\right.$$

$$\left.-\frac{\sqrt{2}\pi}{8}(x^2-w^2)\right\} \simeq 0.865\frac{xy^2}{\sqrt{x^2-y^2x^3}}x\sqrt{\ell n x}\left(\frac{\pi}{4}x^2\right)$$

$$= 0.865\frac{\pi}{4}x\sqrt{\ell n x}\frac{y^2}{\sqrt{x^2-y^2}} \tag{47}$$

Therefore, the function $F(x, y, w)$ approaches

$$F(x, y, w) \simeq \left[0.865(\pi/2)x\sqrt{\ell n x}\right]^{-1} \qquad \text{for high } \phi_p \tag{48}$$

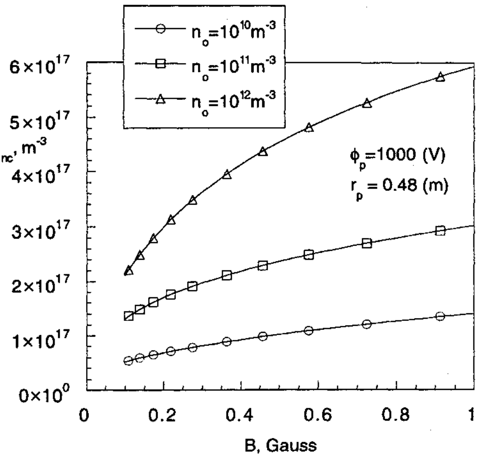

Fig. 6 **Critical neutral density n_{nc} against magnetic field strength B for different plasma densities n_o.**

Originally these two dominant terms come from $\partial n_e/\partial r_s$, i.e., the increase of the electron density due to the increase of r_s. From Eq. (25), the electron density increases as the sheath radius r_s increases because the entrance of the flux tube for the trapped electrons at $z = z_s$ widens. The increase of the electron density affects the sheath explosion in two opposite ways. It increases the negative charge inside the sheath and prevents the sheath from expansion. This is the effect in the numerator of $F(x, y, w)$. At the same time, it increases the positive charge by producing more secondary ions and helps the sheath to expand; this effect is included in the denominator. Because the secondary ion density inside the sheath is proportional to the electron density [see Eq. (16)], these two effects cancel each other. Then the critical neutral density approaches

$$n_{nc} = 0.74\frac{1}{\langle\sigma_i v_e\rangle_o}\sqrt{\frac{2e\phi_p}{m_{si}}}\frac{1}{r_s\,\ell n(r_s/r_p)} \qquad \text{for high } \phi_p \tag{49}$$

Because the sheath radius r_s increases as ϕ_p increases, this leaves little dependence on ϕ_p and the critical neutral density remains nearly constant at high ϕ_p. The critical neutral density stays in the very narrow range for the three plasma densities. It stays between $n_{nc} = 1\times10^{17}$ m^{-3} and $n_{nc} = 4\times10^{17}$ m^{-3} for $200\text{ V} < \phi_p < 1000\text{ V}$. It is lower for the lower plasma density, because the sheath radius r_s is larger for the lower plasma density.

To investigate the dependence of n_{nc} on the other parameters, I plot n_{nc} against B for the three plasma densities at $\phi_p = 1000$ V in Fig. 6. The critical neutral density increases as the magnetic field strength increases. This is because the stronger B (and higher ω_{ce}) bounds the electron motion more strictly and prevents electrons from moving radially. Therefore, it increases n_e as indicated in Eq. (25). The increase of n_e leads to a decrease of r_s. This can be seen by looking at Eq. (45). The decrease of r_s leads to the increase of n_{nc} from Eq. (49).

The critical neutral density decreases slightly as r_p increases. This comes from the factor $\surd[\ell n(r_s/r_p)]$ in Eq. (49). However, at larger $r_p \sim 5$ m this factor changes little and the dependence of n_{nc} on r_p is small. From the dependence of the critical neutral density on four parameters—ϕ_p, n_o, B, and r_p—it is concluded that the critical neutral density lies between a narrow range of $6 \times 10^{16} \sim 6 \times 10^{17}$ m^{-3} for a surface potential less than 1000 V.

Conclusion

Use of high power in future space missions calls for high-voltage power generation and transmission, typically higher than 100 V. The operation at high voltage may cause serious interaction between the spacecraft body and the surrounding plasma. I have studied the electric sheath structure around a cylindrical body with a finite length, which has a high positive potential in magnetized nonflowing ionospheric plasma. The cylindrical body simulates a spacecraft in low Earth orbit, although its orbital motion is neglected. In this paper, I have focused on how the sheath structure changes as the neutral density around the body increases.

The MC-PIC simulation has shown that the sheath boundary increases as ionization occurs inside the sheath. This is because the charge balance inside the sheath is broken as slowly moving secondary ions are produced by ionization. The sheath expands outward to compensate for the relative loss of negative charge by collecting more electrons from the ambient plasma. The expansion of the sheath increases the probability of ionization further by increasing the path length for electrons to travel inside the sheath. Therefore, there is a positive feedback mechanism to expand the sheath boundary and to create a critical neutral density above which the rate of ionization is so large that the sheath expands infinitely.

Theoretical formulation has been done to express the critical neutral density as a function of a set of given parameters, such as cylinder radius, surface potential, magnetic field strength, plasma density, and ionization collision cross section. The theoretical results have been compared with the results of MC-PIC simulations, which serves as a numerical experiment to check the validity of various assumptions made to derive a simple formula to calculate the critical neutral density. The theoretical results agree with the simulation results within a factor of 3 for high surface potentials, i.e., >200 V. The theoretical formula predicts that the critical neutral density depends little on the surface potential and the cylinder radius. It also predicts that the critical neutral density increases as the magnetic field increases. From the parametric study, it is concluded that the critical neutral density lies in a narrow range of $6 \times 10^{16} \sim 6 \times 10^{17}$ m^{-3} for a potential of less than 1000 V.

The results presented in this paper have limitations in two ways. One is that I have studied only the case where the magnetic field is parallel to the cylinder axis. Because I have studied a cylinder geometry whose diameter is comparable to its length, the extension to a spherical geometry would produce results little different from this paper. The case where the magnetic field is perpendicular to the axis of a long cylinder, such as the case of an electrodynamic tether, however, is a very interesting subject and is left for future work. The other limitation of this paper is that I have considered only nonflowing plasma. When these results are applied to the design of real spacecraft, there are serious limitations because spacecraft motion is not taken into account. Nevertheless, the theoretical formulation presented in this paper can be used as a first step to study a more realistic situation in the future.

Appendix: Derivation of Equations (36) and (37)

From the definition of $\psi(x,\xi)$ in Eq. (34), the first integral in the denominator of Eq. (33) is written as

$$\int_1^x \int_1^\xi \frac{\xi'}{\sqrt{\psi(x,\xi') - \psi(x,\xi)}}\,\mathrm{d}\xi'\,\mathrm{d}\xi = H_1(x)$$

$$= \int_1^x \left\{ \int_1^\xi \frac{\xi'}{\sqrt{x^2 \ln(\xi/\xi') + [(\xi'^2 - \xi^2)/2]}}\,\mathrm{d}\xi' \right\} \mathrm{d}\xi \tag{A1}$$

I first change ξ' to $\zeta = \xi'^2/\xi^2$. Then the inner integral becomes

$$\int_1^\xi \frac{\xi'}{\sqrt{x^2 \ln(\xi/\xi') + [(\xi'^2 - \xi^2)/2]}}\,\mathrm{d}\xi'$$

$$= \frac{\sqrt{2}}{2}\xi \int_{1/\xi^2}^{1} \frac{1}{\sqrt{-(x^2/\xi^2)\ln\zeta + \zeta - 1}}\,\mathrm{d}\zeta \tag{A2}$$

The function $1/\sqrt{[-(x^2/\xi^2)\ln\zeta + \zeta - 1]}$ increases very rapidly at $\zeta \sim 1$ as the denominator approaches 0. Therefore, it is sufficient to consider the contribution only near $\zeta \simeq 1$, and I rewrite

$$\int_1^\xi \frac{\xi'}{\sqrt{x^2 \ln(\xi/\xi') + [(\xi'^2 - \xi^2)/2]}}\,\mathrm{d}\xi'$$

$$\simeq \frac{\sqrt{2}}{2}\xi \int_{1-\delta}^{1} \frac{1}{\sqrt{-(x^2/\xi^2)\ln\zeta + \zeta - 1}}\,\mathrm{d}\zeta \tag{A3}$$

where δ is determined later. At $\zeta \simeq 1$, I can write $\ln\zeta \simeq \zeta - 1$ and the preceding integral is simplified to

$$\int_1^\xi \frac{\xi'}{\sqrt{x^2 \ln(\xi/\xi') + [(\xi'^2 - \xi^2)/2]}}\,\mathrm{d}\xi'$$

$$\simeq \frac{\sqrt{2}}{2}\xi \int_{1-\delta}^{1} \frac{1}{\sqrt{-(x^2/\xi^2)(\zeta - 1) + \zeta - 1}}\,\mathrm{d}\zeta$$

$$= \frac{\sqrt{2}}{2}\frac{\xi^3}{x^2 - \xi^2} 2\sqrt{\left(\frac{x^2}{\xi^2} - 1\right)\delta} = \sqrt{2\delta}\frac{\xi^2}{\sqrt{x^2 - \xi^2}} \tag{A4}$$

I substitute this into Eq. (A1) and obtain

$$H_1(x) \simeq \sqrt{2\delta} \int_1^x \frac{\xi^2}{\sqrt{x^2 - \xi^2}} \tag{A5}$$

This integral can be evaluated exactly to

$$\int_1^x \frac{\xi^2}{\sqrt{x^2 - \xi^2}} = \left(-\sqrt{x^2 - \xi^2}\xi\right)_1^x + \int_1^x \sqrt{x^2 - \xi^2}\,\mathrm{d}\xi$$

$$= \sqrt{x^2 - 1} + x^2 \int_{\sin^{-1}(1/x)}^{\pi/2} \cos\theta\cos\theta\,\mathrm{d}\theta$$

$$= \frac{1}{2}\sqrt{x^2 - 1} + \frac{\pi}{4}x^2 - \frac{x^2}{2}\sin^{-1}\frac{1}{x} \tag{A6}$$

Finally

$$H_1(x) \simeq \sqrt{2\delta}\left[\tfrac{1}{2}\sqrt{x^2 - 1} + (\pi/4)x^2 - (x^2/2)\sin^{-1}(1/x)\right] \tag{A7}$$

If I substitute $\delta = 0.374$, the values given by Eq. (A7) agree with the values of $H_1(x)$ given by numerically integrating the original equation [Eq. (A1)] within an error of 2% for $x > 4$. The disagreement gets worse for smaller x; it is still only 5% for $3 < x < 4$ and 9% for $2.5 < x < 3$ and 17% even for $2 < x < 2.5$.

Likewise, the second integral in the denominator of Eq. (33) is written as

$$\int_w^x \int_w^\xi \frac{\xi'}{\sqrt{\psi(x,\xi') - \psi(x,\xi)}}\,\mathrm{d}\xi'\,\mathrm{d}\xi$$

$$= H_2(x) = \int_w^x \left\{ \int_w^\xi \frac{\xi'}{\sqrt{x^2 \ln(\xi/\xi') + [(\xi'^2 - \xi^2)/2]}}\,\mathrm{d}\xi' \right\} \mathrm{d}\xi \tag{A8}$$

By changing ξ' to $\zeta = \xi'^2/\xi^2$, the inner integral becomes

$$\int_w^\xi \frac{\xi'}{\sqrt{x^2 \ln(\xi/\xi') + [(\xi'^2 - \xi^2)/2]}}\,\mathrm{d}\xi'$$

$$= \frac{\sqrt{2}}{2}\xi \int_{w^2/\xi^2}^{1} \frac{1}{\sqrt{-(x^2/\xi^2)\ln\zeta + \zeta - 1}}\,\mathrm{d}\zeta \tag{A9}$$

I look at the fact that $w = r_I/r_p$ is close to $x = r_s/r_p$ for a large potential, and I am evaluating the integral only for $w < \xi < x$. Then, I approximate $\ln\zeta$ by $\ln\zeta \sim \zeta - 1$ between $w^2/\xi^2 < \zeta < 1$. Then I can evaluate the integral exactly to

$$H_2(x) \simeq \int_w^x \frac{\sqrt{2}}{2}\xi \int_{w^2/\xi^2}^{1} \frac{1}{\sqrt{[1 - (x^2/\xi^2)](\zeta - 1)}}\,\mathrm{d}\zeta$$

$$= \int_w^x \frac{\sqrt{2}}{2}\xi\left(2\frac{\sqrt{\xi^2 - w^2}}{\sqrt{x^2 - \xi^2}}\right)\mathrm{d}\xi = \sqrt{2}\int_w^x \frac{\xi\sqrt{\xi^2 - w^2}}{\sqrt{x^2 - \xi^2}}\,\mathrm{d}\xi$$

$$= \frac{\sqrt{2}}{2}\int_0^{\sqrt{x^2 - w^2}} \frac{s^2}{\sqrt{(x^2 - w^2) - s^2}}\,\mathrm{d}s = \frac{\sqrt{2}\pi}{8}(x^2 - w^2) \tag{A10}$$

References

[1]Cho, M., "Sheath Structure Around a High-Voltage Body in Magnetized Nonflowing Ionospheric Plasma," *Journal of Spacecraft and Rockets*, Vol. 35, No. 1, 1998, pp. 82–89.

[2]Wulf, E., and Zahn, U., "The Shuttle Environment: Effects of Thruster Firings on Gas Density and Composition in the Payload Bay," *Journal of Geophysical Research*, Vol. 91, No. A3, 1986, pp. 3270–3278.

[3]Cho, M., "Ionosphere Ionization Effects on Sheath Structure Around a High-Voltage Spacecraft," *Journal of Spacecraft and Rockets*, Vol. 32, No. 6, 1995, pp. 1018–1026.

[4]Cooke, D. L., and Katz, I., "Ionization-Induced Instability in an Electron Collecting Sheath," *Journal of Spacecraft and Rockets*, Vol. 25, No. 2, 1988, pp. 132–138.

[5]Singh, N., and Jaggernauth, A., "Ionization-Driven Plasma Dynamics in a High Voltage Sheath of a Conducting Body in the Ionosphere," *Journal of Geophysical Research*, Vol. 101, No. A8, 1996, pp. 17229–17242.

[6]Hastings, D. E., and Garrett, H., *Spacecraft Environment Interactions*, Cambridge Univ. Press, Cambridge, England, UK, 1996, p. 120.

[7]Hayashi, M., "Electron Collision Cross-Sections for Atoms and Molecules Determined from Beam and Swarm Data," *Atomic and Molecular Data for Radiotherapy, Proceedings of an IAEA Advisory Group Meeting* (Vienna), Rept. IAEA-TECDOC-506, International Atomic Energy Agency, 1988, pp. 193–199.

[8]Cho, M., and Hastings, D. E., "Computer Particle Simulation of High Voltage Solar Array Arcing Onset," *Journal of Spacecraft and Rockets*, Vol. 30, No. 2, 1992, pp. 189–201.

[9]Cho, M., and Hastings, D. E., "An Analytical and Particle Simulation Study of Localized Semi-Vacuum Gas Breakdown Phenomena on High Voltage Solar Surfaces in Low Earth Orbit," *Physics of Fluids B*, Vol. 4, No. 8, 1992, pp. 2614–2625.

[10]Parker, L. W., and Murphy, B. L., "Potential Buildup on an Electron-Emitting Ionospheric Satellite," *Journal of Geophysical Research*, Vol. 72, No. 5, 1967, pp. 1631–1636.

R. G. Wilmoth
Associate Editor